Pendular alignment and strong chemical binding are induced in helium dimer molecules by intense laser fields

Qi Wei[a,b,c,1], Sabre Kais[b,c], Tomokazu Yasuike[d,e], and Dudley Herschbach[f,g,1]

[a]State Key Laboratory of Precision Spectroscopy, East China Normal University, 200062 Shanghai, China; [b]Department of Chemistry, Purdue University, West Lafayette, IN 47907; [c]Birck Nanotechnology Center, Purdue University, West Lafayette, IN 47907; [d]Department of Liberal Arts, The Open University of Japan, 261-8586 Chiba, Japan; [e]Elements Strategy Initiative for Catalysts and Batteries, Kyoto University, 615-8520 Kyoto, Japan; [f]Department of Physics, Texas A&M University, College Station, TX 77843; and [g]Department of Chemistry and Chemical Biology, Harvard University, Cambridge, MA 02138

Contributed by Dudley Herschbach, July 29, 2018 (sent for review June 20, 2018; reviewed by Nimrod Moiseyev and Mitchio Okumura)

Intense pulsed-laser fields have provided means to both induce spatial alignment of molecules and enhance strength of chemical bonds. The duration of the laser field typically ranges from hundreds of picoseconds to a few femtoseconds. Accordingly, the induced "laser-dressed" properties can be adiabatic, existing only during the pulse, or nonadiabatic, persisting into the subsequent field-free domain. We exemplify these aspects by treating the helium dimer, in its ground ($X^1\Sigma_g^+$) and first excited ($A^1\Sigma_u^+$) electronic states. The ground-state dimer when field-free is barely bound, so very responsive to electric fields. We examine two laser realms, designated (I) "intrusive" and (II) "impelling." I employs intense nonresonant laser fields, not strong enough to dislodge electrons, yet interact with the dimer polarizability to induce binding and pendular states in which the dimer axis librates about the electric field direction. II employs superintense high-frequency fields that impel the electrons to undergo quiver oscillations, which interact with the intrinsic Coulomb forces to form an effective binding potential. The dimer bond then becomes much stronger. For I, we map laser-induced pendular alignment within the X state, which is absent for the field-free dimer. For II, we evaluate vibronic transitions from the X to A states, governed by the amplitude of the quiver oscillations.

laser-induced properties | pendular alignment | quiver oscillations | chemical bonding | Kramers–Henneberger approximation

The $^4He_2$ dimer, in its ground electronic state and field-free, is extremely fragile. Although its potential energy curve has appreciable well depth (Fig. 1*A*), the vibrational zero-point energy is nearly equal. Hence, the sole bound vibrational state lies only slightly below the separated atoms asymptote. The vibrational wavefunction thus extends far beyond the classical turning point, making the dimer extremely bloated. Its average internuclear distance is about 20× longer than that at the well minimum. With 80% probability, the two nuclei of the dimer reside outside the classically forbidden region. Determining accurately these properties has been a 25-y odyssey that led to exquisite advances in both theory (1–3) and experiments (4–8). A kindred subfield has developed, which treats "long-range" diatomic molecules, weakly bound in vibrational states that lie not far below the dissociation asymptote (9). Such states qualify as "quantum halos" as the vibrational wavefunction tunnels far into classically forbidden regions (10). Recently, the He_2 ground-state halo wavefunction has been imaged with remarkable accuracy by extraordinary experiments using a Coulomb explosion technique (8).

Further field-free micro- and macroscopic properties of the ground X state of He_2 have been studied (11). Also, field-free spectra have been obtained for several excited electronic states, particularly the A state (12). Previous theoretical work, applying superintense pulsed-laser fields (realm II) to ground-state He_2 has predicted formation of a strong chemical bond (13–15). However, the induced bond exists just during the pulse duration and experimental confirmation is as yet lacking. Here we treat theoretical aspects that bring out features amenable to experimental observation. These include treating less intense laser fields (realm I), which can provide pendular alignment and spectra (16–20), and treating the A state in addition to the X state (in realm II) to obtain vibronic spectra.

Unless explicitly otherwise, we use atomic units: 1 a.u. for distance is a bohr unit (0.0529 nm); for time 2.42×10^{-17} s; for mass 9.11×10^{-25} kg; for energy a hartree unit (27.2 eV; equivalent to 3.16×10^5 kelvin); for laser intensity 3.51×10^{16} $\mathrm{Wcm^{-2}}$; and for laser frequency 6.58×10^{15} Hz, corresponding to wavelength of 45.5 nm.

Realm I: Laser Interactions with Molecular Polarizability

In this realm, the external laser field is less strong than the internal Coulombic forces that govern the electronic structure within a molecule. Laser fields then perturb the electronic structure of a typical molecule chiefly via its polarizability (16–21). For a nonpolar diatomic molecule with polarizability components $\alpha_{||}$ and $\alpha_\perp$ parallel and perpendicular to the molecular axis, subjected to plane-wave radiation of nonresonant frequency ω with electric field strength, $\varepsilon = \varepsilon_0 \cos\omega t$, the interaction potential is

$$V_\alpha(R,\theta) = -1/2\varepsilon^2 g(t)\left[\Delta\alpha\cos^2\theta + \alpha_\perp\right]. \qquad [1]$$

Here $g(t)$ is the time profile of the laser pulse with peak intensity $I = \varepsilon^2$. For a Gaussian profile, $g(t) = \exp[-4\ln(2)t^2/\tau^2]$, the full width at half maximum τ is termed the pulse duration. For

Significance

Intense electric fields, provided by pulsed lasers, can profoundly alter the electronic structure of atoms and molecules. For the helium dimer, we carry out a theoretical study of laser interactions in two realms: (I) fields not strong enough to dislodge electrons, but interact with the anisotropic polarizability to induce spatial alignment of the molecular axis; and (II) superintense, high-frequency lasers that impel electrons to undergo quiver oscillations that interact with the intrinsic Coulomb forces and induce an extremely strong chemical bond. By including in II an excited electronic state, we bring out features amenable to experimental observation that has been lacking.

Author contributions: Q.W., S.K., T.Y., and D.H. designed research; Q.W., T.Y., and D.H. performed research; Q.W., S.K., and D.H. analyzed data; and Q.W. and D.H. wrote the paper.

Reviewers: N.M., Technion Israel Institute of Technology; and M.O., California Institute of Technology.

The authors declare no conflict of interest.

[1]To whom correspondence may be addressed. Email: qwei@admin.ecnu.edu.cn or dherschbach@gmail.com.

www.pnas.org/cgi/doi/10.1073/pnas.1810102115

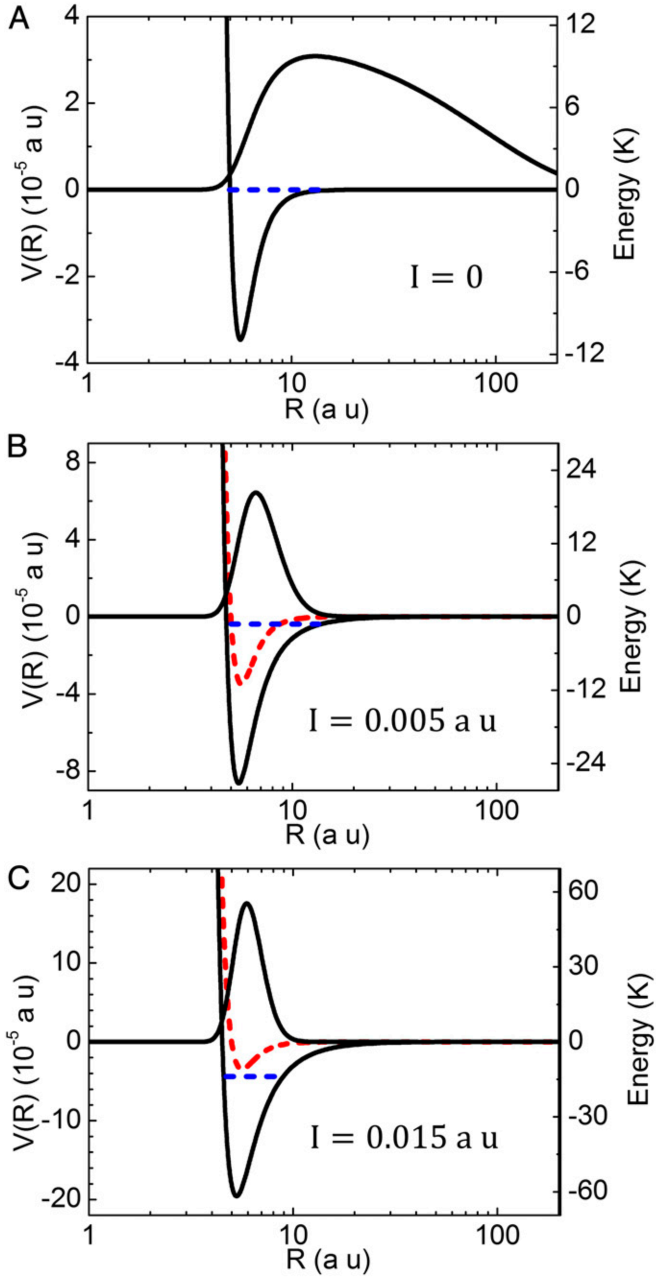

Fig. 1. Ground electronic state $X^1\Sigma_g^+$ of $^4He_2$ dimer. (*A*) Field-free dimer potential energy curve (1–3). Well depth $V(R_m) = 3.5 \times 10^{-5}$ a.u. (11 K) at $R_m = 5.61$ a.u. Sole vibrational energy level (dashed blue) $E_0 = -4.1 \times 10^{-9}$ a.u. (−1.3 mK) is only slightly below asymptote for separated atoms. Probability distribution of internuclear distance (black, arbitrary units), $R^2|\Psi_{vib}(R)|^2$, extends beyond 100 a.u. Expectation value for internuclear distance $\langle R \rangle$ = 104 a.u. (*B*) Laser field (I = 0.005 a.u.)-induced alteration of potential energy curve (compared with free-field, dashed red), with downward shift of sole pendular–vibrational level ($|000\rangle$, dashed blue). (*C*) For stronger laser field (I = 0.01 a.u.). In *B* and *C*, the radial curves shown pertain to $\theta = 0°$, whereas the penvib levels incorporate ranges of both *R* and θ; see Fig. 3 and Table 2.

nonresonant frequencies much greater than the reciprocal of the laser pulse duration, $\omega \gg 1/\tau$, averaging over the pulse period converts ε^2 to $\varepsilon_0^2/2$. The dependence on the angle θ between the molecular axis and the electric field direction is governed by the anisotropy $\Delta\alpha = \alpha_{\|} - \alpha_{\perp}$ of the polarizability. The term $\Delta\alpha\cos^2\theta$ introduces an equatorial barrier that quenches rotation but allows the molecular axis to undergo pendular libration about the electric field direction. The internuclear distance *R* enters implicitly as a parameter in the polarizability components. Also, we note that spectra governed by molecular polarizability have the same selection rules as the Raman effect (22); for a diatomic rotor, $\Delta J = \pm 2,0$.

Before outlining calculations, we exhibit results for the ground-state helium dimer, resulting from Eq. **1**, the interaction potential. Fig. 1 contrasts laser-induced changes (Fig. 1 *B* and *C*) in radial vibrational potential energy curves with the field-free case (Fig. 1*A*). The well depths are substantially deepened, along with consequent lowering of the sole bound level, which is properly designated a pendular–vibrational level (dashed blue). That lowering is accompanied by retreating of the probability distributions of the bond length. The radial potential curves and "penvib" levels shown incorporate θ, the alignment angle. Fig. 2*A* displays the dependence of the polarizability components on the internuclear distance. Fig. 2*B* exhibits the angular barrier imposed by the anisotropy of the polarizabilty, via $\Delta\alpha\cos^2\theta$. Fig. 3 presents 2D potential energy surfaces and wavefunctions to bring out the joint dependence of angular alignment along with the internuclear distance. Fig. 4 shows the dependence on the laser intensity (in Fig. 4*A*) of the penvib levels and (in Fig. 4*B*) of

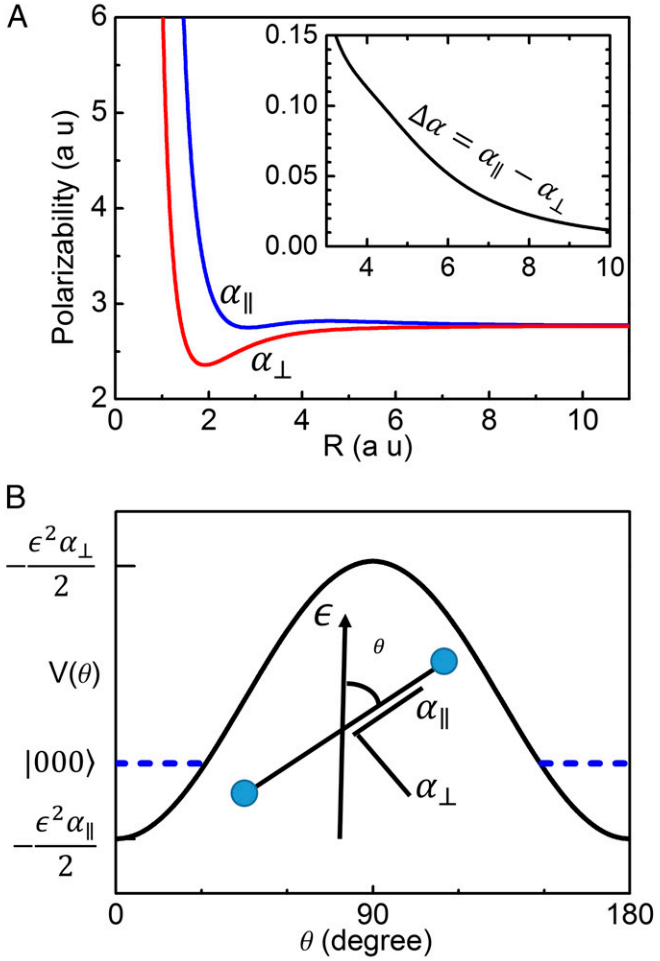

Fig. 2. Quantities involved in interaction potential, Eq. **1**, for ground-state helium dimer. (*A*) Dependence of polarizability components on internuclear distance. (*Inset*) Anisotropy is shown. (*B*) Laser-induced angular alignment of the dimer axis (schematic sketch). Potential minima in the polar regions, near $\theta = 0°$ and 180°, are separated by an equatorial barrier that quenches end-for-end rotation. Location of lowest penvib level is indicated by $|000\rangle$ (dashed blue).

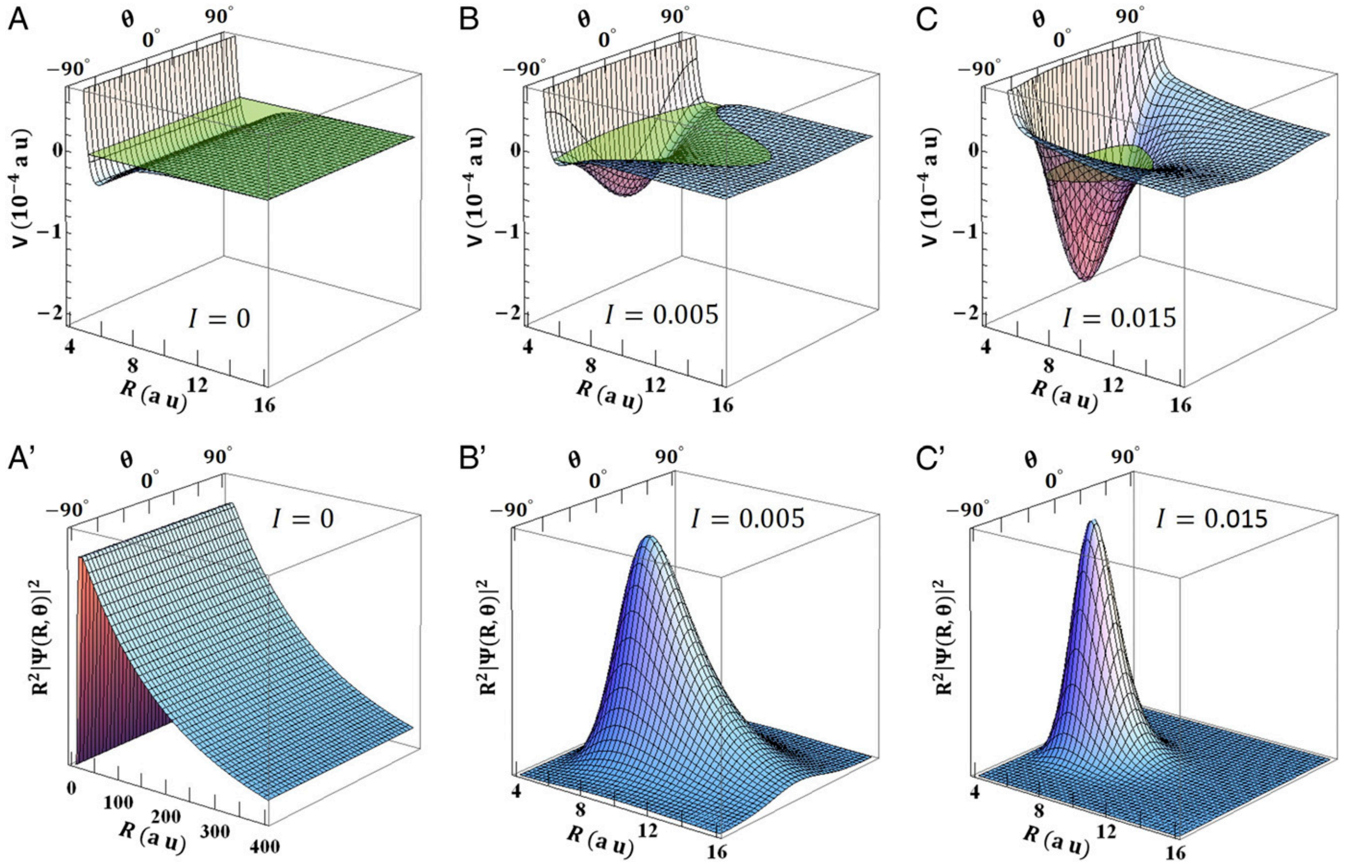

Fig. 3. Two-dimensional plots exhibiting radial and angular dependence, corresponding to Fig. 1. (*A*–*C*) Potential energy surfaces with transparent planes (green) that depict location of the lowest penvib quantum level. (*A′*–*C′*) Probability distributions, $R^2|\Psi(R,\theta)|^2$, square of wavefunctions weighed by the radial Jacobian factor.

$\langle\cos^2\theta\rangle$ and the pendular alignment range, $\Delta\theta$, which narrows as the laser intensity is increased.

Incorporating the interaction potential requires treating the full Hamiltonian,

$$H = H_{\mathrm{vib}} + H_{\mathrm{rot}} + V_\alpha(R,\theta), \qquad \textbf{[2]}$$

wherein the vibrational and rotational terms have the familiar field-free form:

$$H_{\mathrm{vib}} = -1/2\,\mu\,\mathrm{d}^2/\mathrm{d}R^2 + V_0(R); H_{\mathrm{rot}} = BJ^2, \qquad \textbf{[3]}$$

with μ ($= m_{\mathrm{He}}/2 = 3{,}675$ a.u.) the reduced mass, $V_0(R)$ the field-free radial potential, and $B = 1/(2\ \mu R^2)$ the rotational constant. To obtain the penvib states from Eq. **2**, we applied a stepwise iterative method. Step 1 sets $\cos^2\theta$ and J^2 as zero, temporarily. Then R is the only variable, so a radial wavefunction Ψ_R is readily obtained by conventional means. In step 2, a given R is taken as constant with θ and J^2 variable, and a pendular wavefunction Ψ_θ is obtained. The process is repeated for many values of R. In step 3, the product $\Psi_R\Psi_\theta$ is used to calculate the expectation values $\langle\cos^2\theta\rangle$ and $\langle J^2\rangle$ and the energy levels. These are inserted into the full Hamiltonian and the whole procedure is iterated until the quantities obtained in step 3 converge; typically seven or eight iterations yield six-digit agreement.

The laser pulse duration has a key role (19–21). Fig. 5*A* displays the variation with laser intensity of the helium dimer rotational period π/B along with contrasting shorter and longer pulse durations. Also shown is the constraint imposed by the ionization half-life $T_{1/2}$ as estimated from atomic helium data (23). For example, for I ~ 0.01 a.u., $\pi/B \sim 25$ ps and $T_{1/2} \sim 10$ ps. The designated pulse durations $\pi/5B$ and $5\pi/B$ approach limits: nonadiabatic and adiabatic.

If the pulse is much shorter than π/B, the molecule is left in a coherent superposition of rotational eigenstates. Such an impulsive pulse can yield nonadiabatic behavior: The molecule retains the imparted pendular alignment and angular momentum after the laser pulse has passed. For He_2, due to its extremely weak bond, the impulsive pulse can result in dissociation from "shaking" or "kicking" imposed by the centrifugal angular momentum (24–26). This situation has been recently experimentally demonstrated (27). Such dissociation can occur whenever vibrational motion is unperturbed or slightly so, and the retained centrifugal energy exceeds the gap between the highest field-free vibrational level and the dissociation asymptote.

If the laser pulse is much longer than π/B, the molecule is adiabatically guided into pendular states but emerges from the pulse unchanged from the initial field-free state. Hence, the induced penvib states need to be observed midway in the pulse via a pump–probe technique. However, a hybrid technique is available (21, 28). The laser field can be adiabatically turned on, producing the penvib states, then suddenly turned off. The adiabatically prepared states can then dephase and rephase to form the same revival output that would be obtained from an impulsive pulse.

As shown in Fig. 5*B*, with increasing laser intensity depletion by ionization sets in much more drastically for the adiabatic and hybrid modes than for the impulsive mode. Up to $I = 0.005$ a.u., the dimer molecules that survive ionization are estimated to exceed 90% for all three pulse modes. But, by $I = 0.010$ a.u. the

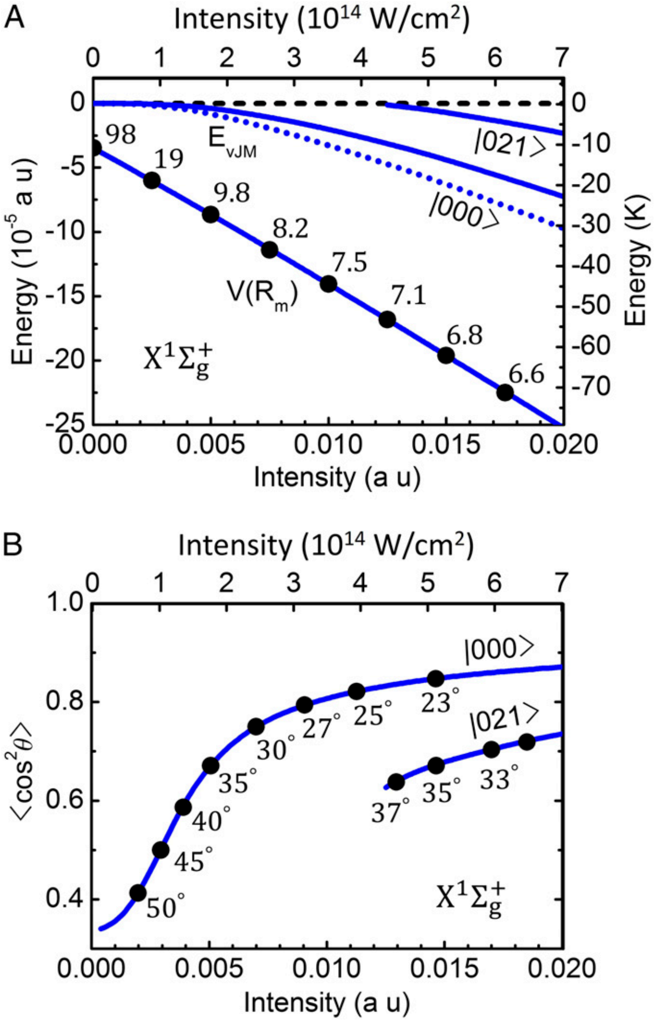

Fig. 4. Variation with laser intensity of properties of ground-state helium dimer. (*A*) The laser-induced bound penvib levels $E_{vJM} = |000\rangle$ and $|021\rangle$ (blue) include the contribution from the centrifugal term, $\langle BJ^2\rangle$, in Eq. **2**. The dotted curve shows where the $|000\rangle$ level would be if the centrifugal term were omitted. Also shown is the potential depth $V(R_m)$. Numbers close to points indicate the averaged internuclear distance $\langle R\rangle$; compare Fig. 1 *B* and *C* and Table 2. (*B*) Expectation values $\langle\cos^2\theta\rangle$ for the penvib levels (blue). Also indicated ($\pm\Delta\theta$, black points) are angular amplitudes of the pendular librations, $\Delta\theta = \arccos\langle\cos^2\theta\rangle^{1/2}$.

survival has fallen below $10^{-3}\%$ for the adiabatic and hybrid modes, yet holds up to ~60% for the impulsive mode. Furthermore, at $I = 0.015$ a.u. the impulsive survival remains at ~15%. Since ionized molecules can be readily deflected away, the surviving molecules can be readily recorded down to 1%, so the practical border for realm I occurs near $I = 0.008$ a.u. for the adiabatic mode and beyond $I = 0.020$ a.u. for the impulsive mode.

The laser-induced properties of He_2 predicted in Fig. 4 thus are accessible for the impulsive mode. The $|000\rangle$ penvib level is lowered enough by the laser interaction to offset the extra centrifugal energy, thus avoiding dissociation. Likewise, the $|021\rangle$ level also becomes bound when the laser intensity climbs above 0.013 a.u. (The $|020\rangle$ and $|022\rangle$ levels remain unbound until the laser intensity exceeds 0.030 a.u.) The transition between $|000\rangle$ and $|021\rangle$ levels offers a compelling test. It occurs in the millimeter wave region, ranging from 6–11 cm^{-1} (180–330 GHz) for laser intensity from 4–7×10^{14} W/cm^2 (0.01–0.02 a.u.). Suitable probe lasers for this region are available (29). Lower limit of probe pulse duration ranges from 3 to 5 ps. The alignment of the dimer axis, recorded by $\langle\cos^2\theta\rangle$, provides another test, accessible by particle-imaging techniques (30).

Realm II: Laser Disruption of Electronic Structure

In this realm the laser field is superintense, comparable to the intrinsic Coulomb binding forces, and well above the threshold for ionization. However, theory and computer simulations predict that in this regime the ionization probability decreases as the laser intensity increases (31–33). This apparent paradox occurs because the laser-dressed molecule acquires an effective binding potential for the electrons by interaction of the rapidly oscillating laser field with the Coulombic potential. The stabilization against ionization even extends to multiply charged anions of hydrogen (34) and anions of other atoms (35–37), as well as

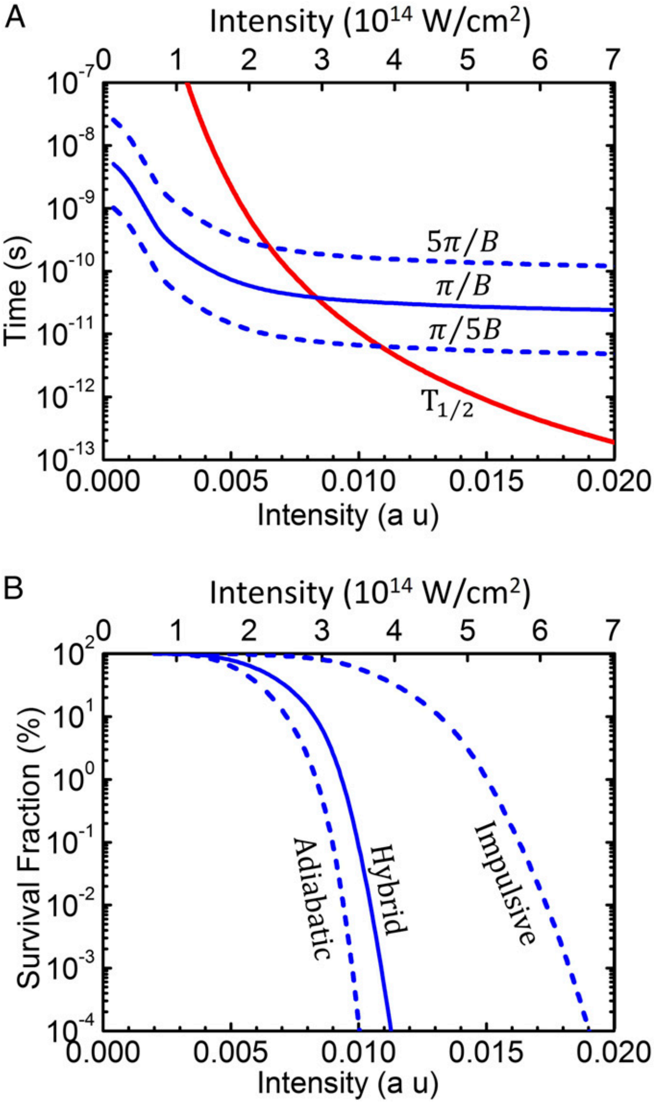

Fig. 5. Variation with laser intensity of pulse options. (*A*) Helium dimer rotational period, π/B (blue curve), along with dashed curves that indicate shorter and longer pulse durations: $T_{pd} = \pi/5B$ and $5\pi/B$, respectively for nonadiabatic and adiabatic options. Also shown is the ionization half-life (red curve) of atomic helium, $T_{1/2} = \ln 2/\Gamma$, derived from single-electron ionization rates, for laser fields of wavelength 780 nm, obtained from accurate theoretical data of ref. 23. (*B*) Estimated fraction (%) of dimer molecules surviving ionization after undergoing laser pulses: $\exp(-0.6931T_{pd}/T_{1/2})$.

positronium (38) and some simple diatomic molecules (13–15, 39). Even more striking is a theoretical demonstration, using a carefully devised laser dressing that counteracts Coulombic repulsion, to form a metastable HD^{2+} molecule (40). That emulates a juggler, balancing a stick on the tip of a finger. Kindred stabilization effects appear in the inverse pendulum of Kapitza (41), in the Paul mass filter (42), and Hau (43) guided matter waves.

The stabilization regime depends on the laser frequency, as well as the laser intensity. When the quiver oscillations of electrons driven by the laser field become dominant, a juggler-like procedure termed high-frequency Floquet theory (HFFT) has provided a good approximation for time averaging (31–33). As a small molecule, such as He_2, is miniscule compared with the wavelength of the laser light, each of its electrons is subject to the same laser field. All then undergo synchronously quiver oscillations,

$$\boldsymbol{a}(t) = \alpha_0 \cos(\omega t)\hat{\mathbf{e}}, \tag{4}$$

along the electric field vector (for linearly polarized light $\hat{\mathbf{e}}$ is a unit vector orthogonal to the propagation direction). The maximum quiver amplitude is $\alpha_0 = E_0/\omega^2$, with ω the frequency and $E_0 = I^{1/2}$ the field amplitude. The HFFT procedure is simplified by adopting a reference frame attached to the quivering electrons, designated the Kramers–Henneberger (KH) frame (44, 45). It is translated by $\boldsymbol{a}(t)$ with respect to the laboratory frame. Hence, in the KH frame the electrons all remain fixed, while instead the nuclei quiver along the $\boldsymbol{a}(t)$ trajectory. Thereby the Coulombic attraction between any electron and a nucleus with charge Z takes the form $-Z/|\boldsymbol{r}_i + \boldsymbol{\alpha}(t)|$. The electrons then feel a time-averaged effective attractive potential, the "dressed" potential, given by

$$V_{\mathrm{KH}}(\boldsymbol{r}_i, \alpha_0) = -\frac{\omega}{2\pi}\int_0^{2\pi/\omega} \frac{Z dt}{|\boldsymbol{r}_i + \boldsymbol{\alpha}(t)|}, \tag{5}$$

where the time average extends over one period of the laser field. There are higher-order frequency-dependent corrections to the dressed potential, which are proved to be small and can be neglected at high frequencies (36).

The HFFT version of the time-independent electronic Schrödinger equation, in accord with the Born–Oppenheimer approximation for a homonuclear diatomic molecule, has the familiar form for a field-free molecule, except for replacing the electron-nucleus terms with the dressed KH potential terms:

$$\sum\nolimits_{i=1}^{N}\left[\frac{1}{2}p_i^2 + V_{\mathrm{KH}}\left(\boldsymbol{r}_i - \frac{\boldsymbol{R}}{2}, \alpha_0\right) + V_{\mathrm{KH}}\left(\boldsymbol{r}_i + \frac{\boldsymbol{R}}{2}, \alpha_0\right)\right.$$
$$\left. + \sum\nolimits_{j=1}^{i-1}\frac{1}{|\boldsymbol{r}_i - \boldsymbol{r}_j|} + \frac{Z^2}{R}\right]\Phi = \epsilon^{(N)}(\alpha_0, \boldsymbol{R})\Phi. \tag{6}$$

The laser intensity and frequency thus appear only in the KH terms and enter only via the quiver amplitude. The energy eigenvalues $\epsilon^{(N)}(\alpha_0, \boldsymbol{R})$ and wavefunctions Φ are functions of the number N of electrons, the quiver amplitude α_0, and the internuclear vector $\boldsymbol{R}$, both its magnitude and its angle θ from the electric field direction. Computational details in evaluating the KH integrals of Eq. **6** are described in previous papers (13–15). We inserted the integrals obtained in ref. 13 into the standard GAMESS program package (46) and employed conventional Hartree–Fock orbitals (restricted Hartree–Fock, RHF, rather than unrestricted HF). For the range of quiver amplitudes that we treated, $\alpha_0 \le 2$, comparisons with accurate numerical calculations verified that this procedure was adequate for the ground electronic state, $X^1\Sigma_g^+$. In treating the first excited electronic state, $A^1\Sigma_u^+$, we augmented the RHF orbitals with a single configuration interaction (CIS) approximation (47). The CIS method is considered to provide a well-balanced description for one-electron exited states compared with an HF ground state.

The pair of KH terms in Eq. **6** can be viewed (48) as the electrostatic potentials generated by two lines of positive charge, depicted in Fig. 6*A*, each of length $2\alpha_0$, parallel to the electric field vector and centered on the nuclei at $\pm R/2$. The electrons hence are attracted to the "smeared-out" lines of the nuclear charges and are most attracted to the quiver endpoints at $\pm\alpha_0$. Consequently, superlaser intensities induce the electron distribution to exhibit dichotomy (49). The dressed Coulombic potentials cluster electrons near the quiver endpoints, as if they were a pair of virtual nuclei separated by $2\alpha_0$. For He_2, the dichotomy is feeble for $\alpha_0 \le 0.2$ and modest for quiver amplitudes below $\alpha_0 \le 2$. At larger amplitudes, the lobes become more widely spaced and foster stabilization by decreasing the ionization rate.

The eigenvalues of Eq. **6** provide the dimer potential energy surfaces: $V(\alpha_0, R, \theta)$. A striking feature, seen in Fig. 6*B*, is that for

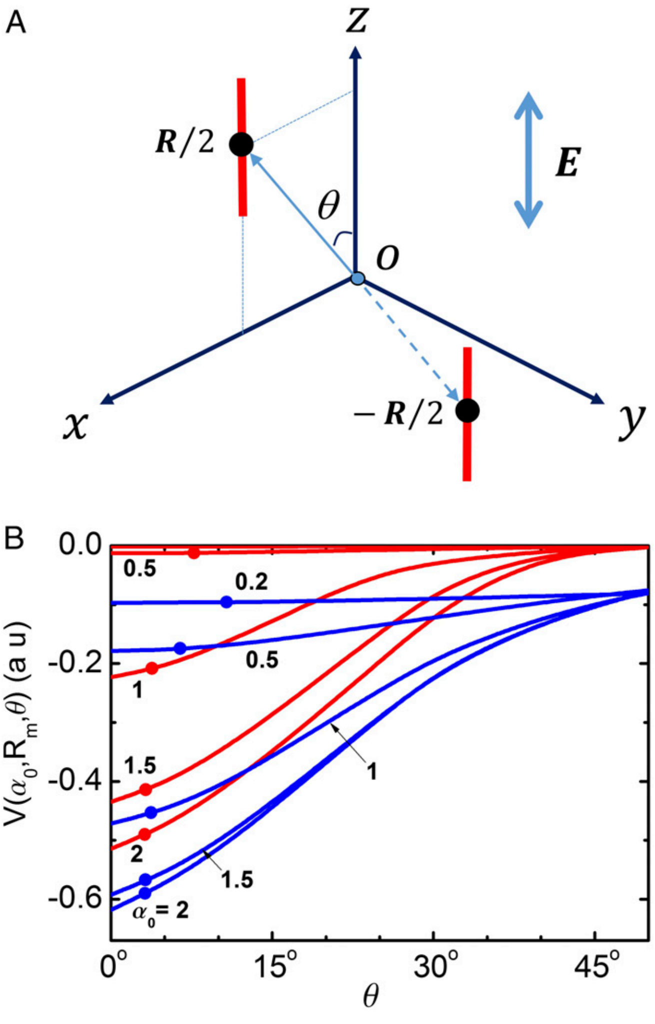

Fig. 6. (*A*) "Lines of charge" generating the effective potential acting on each electron in the V_{KH} terms in Eq. **6**. These line segments of length $2\alpha_0$ are parallel to the laser polarization along the *z* axis (toward unit vector **e** of Eq. **4**) and centered on the nuclei at $\pm R/2$. The internuclear vector ***R*** is directed at angle θ from the *z* axis, here drawn with the azimuth $\phi = 0$ about the *z* axis (eigenproperties do not depend on that uniform angle). (*B*) Variation with θ of potential well depth: $V(\alpha_0, R_m, \theta) = \epsilon^{(4)}(\alpha_0, R_m, \theta) - \epsilon^{(4)}(\alpha_0, \infty, \theta)$, from eigenvalues of Eq. **6**, for X (red) and A (blue) states and for different quiver amplitudes $\alpha_0 = 0.2, 0.5, 1.0, 1.5$ and 2.0 a.u., respectively. Dots indicate, for the lowest penvib levels, the pendular range of the dimer axis at the radial minimum, R_m.

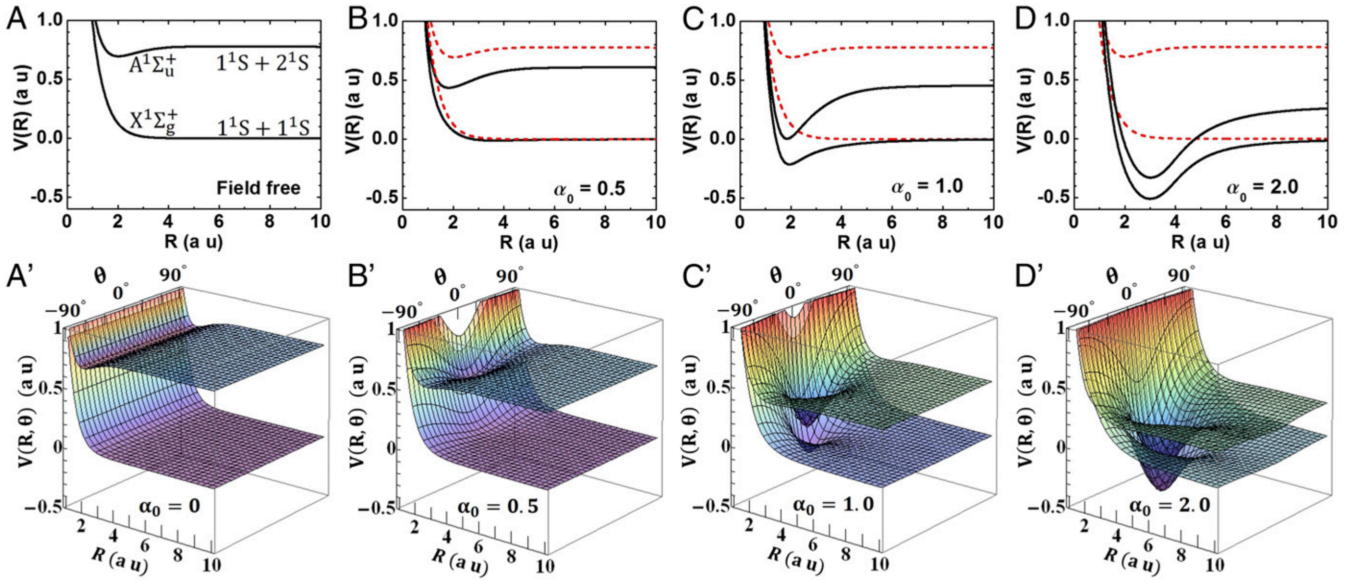

Fig. 7. KH $^4He_2$ dimer potential energy surfaces for both electronic ground-state $X^1\Sigma_g^+$ and excited-state $A^1\Sigma_u^+$, for quiver amplitudes α_0 = 0, 0.5, 1, 2. (*A–D*, *Upper*) shows radial R dependence with optimal alignment ($\theta = 0$) compared with field-free (dashed red); note that the zero for the ordinate energy scale is the asymptote for the ground-state separated atoms. (*A′–D′*, *Lower*) shows 2D plots of *R*, θ dependence (Table 1).

both the X and A states the pendular angular range of the dimer axis is constrained within less than ±10° when $\alpha_0 = 0.5$ and less than ±5° when $\alpha_0 \le 1$, for the lowest penvib levels and $R = R_m$, the potential minimum. Hence, in exploring the KH regime, we usually just set $\theta = 0$. The potential energy surfaces shown in Fig. 7 have set $\theta = 0$ in the upper panels but not in the lower panels. The most dramatic aspect is that with $\alpha_0 \sim$ 1–2 a.u., chemical bonding is drastically enhanced. That had been found previously for the X state (13–15). The A state has substantial bonding when field-free, but we find it also is much enhanced. The results for both X and A states were computed numerically, but the potential curves $V(R, \theta = 0)$ fit tolerably well to the Morse potential,

$$V(R) = D_e\left(e^{-2\beta(R-R_e)} - 2e^{-\beta(R-R_e)}\right). \qquad [7]$$

Table 1 lists the three fitted parameters: β; $D = V(R_m)$, the well depth; and R_m, the location of its minimum. For $\alpha_0 = 2$ a.u., taking the bond strength as about equal to the well depth expressed in a familiar chemical unit, the bonds $D_X = 1{,}300$ and $D_A = 1{,}600$ kJ/mol are extremely strong. Also notable is the large lowering of the asymptote for separated atoms for the A state compared with the X state.

In the eigenenergies obtained from Eq. **6**, the laser intensity and frequency enter only via the quiver amplitude, $\alpha_0 = \sqrt{I}/\omega^2$, but the HFFT criteria (31) impose upper and lower bounds on the pump laser frequency:

$$137/\alpha_0 \gg \omega \gg |\epsilon^{(N)}(\alpha_0, R)| \Big/ N. \qquad [8]$$

The upper bound is required to ensure that both the dipole approximation holds (radiation wavelength large compared with $2\alpha_0$) and a nonrelativistic treatment suffices (maximum quiver speed much lower than the speed of light). The lower bound requires that the field must oscillate much faster than electron motion within the molecule. This is specified by an average excitation energy in the field (48), usually estimated by the energy eigenvalue that appears on the right-hand side of Eq. **6** divided by the number of electrons in the molecule ($N = 4$). As displayed in Fig. 8, the lower bound evaluated at R_m is similar for the X and A states. For the laser intensity, estimates have been made for the X state of $\omega = 10$ at $\alpha_0 = 1.0$ (50) and $\omega = 4$ at $\alpha_0 = 2.5$ (15), but for the A state no estimate is available. Here we presume both states are roughly similar and simply exhibit $\omega = 5$ and 10 (dashed red lines), which are well above the lower bound and below the upper bound, provided that α_0 does not exceed 2 or 3. The corresponding laser intensity (dashed blue curves) increases strongly with increase of the quiver amplitude and even more strongly with the frequency. Consequently, e.g., if $\alpha_0 = 1$ and $\omega = 10$, the requisite laser intensity should be 10^4a.u. $= 3.5 \times 10^{20}$ W/cm^2 with wavelength $\lambda = 45.5/\omega = 4.5$ nm. Such properties can be attained from X-ray free-electron lasers, now accessible in several large facilities (51). Also, promising results obtaining coherent X-rays from high-harmonics generation have emerged from table-top experiments (52).

Illustrative Franck–Condon vibronic transitions between the X and A states are shown in Fig. 9, for $\alpha_0 = 0.5$ and $\alpha_0 = 1$. As seen in Fig. 7 and Table 1, for $\alpha_0 = 0.5$ the radial potential of the X state near $R \sim 2$ is steeply repulsive below a deep well in the A state. Hence, there occurs an internal photodissociation. The emitted transition from $v_A = 0$ reflects from the steep X wall, dissociates the dimer, and travels away as a continuous wave. The atoms fly apart, sharing the kinetic energy, which arises from the height of the impact point on the X potential above the exit asymptote. In contrast, near $R \sim 4$ the X state has a modest well, so either an absorption or emission transition connects the $v_X = 0$ level to the turning point of $v_A = 17$, among other A vibrational

Table 1. Morse fit parameters for KH potential energy curves

$X^1\Sigma_g^+$				$A^1\Sigma_u^+$			
α_0	D_e	R_e	β	α_0	D_e	R_e	β
0.1	0.0002	5.45	0.60	0.1	0.088	2.0	1.30
0.2	0.0012	4.70	0.75	0.2	0.099	1.90	1.20
0.5	0.012	3.62	0.68	0.5	0.18	1.77	1.00
1.0	0.23	1.90	1.10	1.0	0.47	1.83	1.10
1.5	0.43	2.35	0.85	1.5	0.59	2.32	0.80
2.0	0.51	2.95	0.70	2.0	0.62	3.0	0.65

In atomic units; pertain to Fig. 7, *Upper* with $\theta = 0°$.

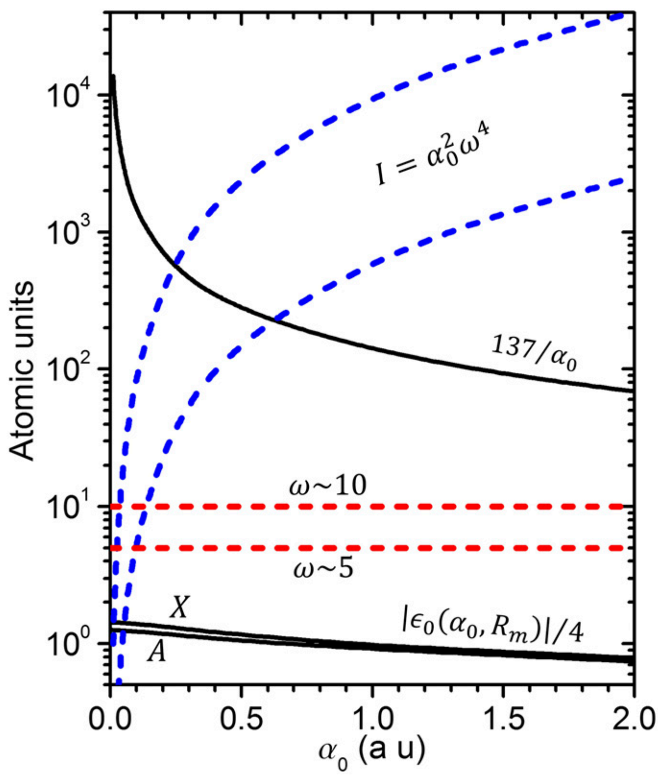

Fig. 8. Criteria of Eq. **8** governing quiver amplitude and specifying lower and upper bounds (black curves) for laser frequency, with trial values ω = 10 and 5 (red dashed lines) and corresponding laser intensity (blue curves).

levels. For $\alpha_0 = 1$, the X state has acquired a deep well near $R \sim 2$ that aligns with the A state well, so both states offer transitions between ladders of discrete vibrational levels.

Our prime interest in the transitions between X and A is considering experiments that can confirm the KH Floquet approach. Much depends on the photoionization lifetime. Theoretical calculations (50) for the X state, when $\alpha_0 \approx 1$ and $\omega = 10$ at fixed $R = R_m$, found the lifetime reached 1 ps at maximum but is very sensitive to R and decreases drastically away from R_m. The lifetime drops to a few femtoseconds for vibrational states. Also, except for the $v_X = 0$ level, transitions (mid-IR region) between the adjacent vibrational state levels were overcome by broadening. In the much larger electronic transitions between X and A (UV region) the lifetimes allow distinct vibrational levels. As seen in Fig. 7, with increasing $\alpha_0 > 0.7$, the energy gap between the X and A potential surfaces decreases markedly. That change should provide clear evidence for KH dressing, available from either an absorption or emission discrete spectrum.

A complementary aspect, with decreasing $\alpha_0 < 0.7$, pursues continuum emission spectra between the A and X potential surfaces, as depicted in Fig. 10*A*. The field-free spectrum, for $\alpha_0 = 0$, is centered at 130×10^3 cm^{-1}. It was observed nearly a century ago among UV continuum bands and soon identified as primarily from the $A^1\Sigma_u^+$ state and named for Hopfield (53). For $\alpha_0 = 0.5$, the continuum band becomes centered at 70×10^3 cm^{-1}. Such a large shift in the spectrum offers a direct experimental test of the KH process. Moreover, the accompanying dissociation of the dimer liberates kinetic energy, as displayed in Fig. 10*B*. That invites another experimental test, detecting trajectories of the emerging helium atoms by means of an imaging technique widely used for photodissociation and reactive molecular collisions (30). At first blush, the predicted distribution of kinetic energy is not much different between $\alpha_0 = 0$ and $\alpha_0 = 0.5$, so the peak exit velocity of the He atoms should be similar. However, in our case of "internal photodissociation," the field-free A state delivers spontaneous emission, with a leisurely lifetime of 0.55 ns (53). Instead, the KH regime is clearly distinct since it uses superintense lasers that deliver stimulated emission with a hasty lifetime below femtoseconds.

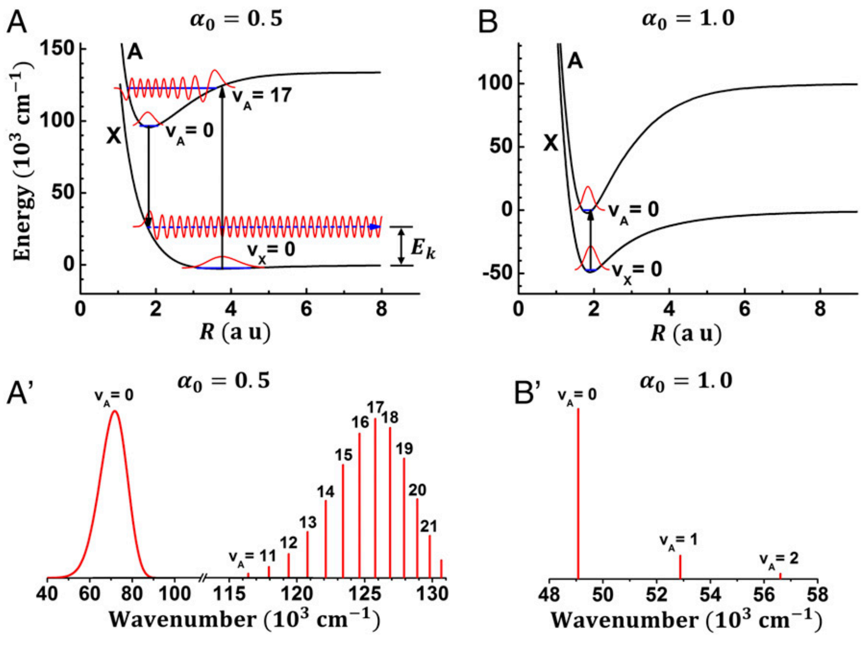

Fig. 9. Franck–Condon transitions between KH potential curves of ground-state $X^1\Sigma_g^+$ and excited-state $A^1\Sigma_u^+$. (*A* and *A′*) For $\alpha_0 = 0.5$. From lowest vibrational level of the A state, $v_A = 0$, transition reflects from the steep repulsive region of the X state, dissociates the dimer, and becomes a continuous traveling wave carrying off kinetic energy. Sample transition from higher level, $v_A = 17$, connects turning point to the lowest vibrational level of the X state. Transition energies (units 10^3 cm^{-1}): continuum peaks at 70, reflecting shape of $v_A = 0$, while discrete lines between 116 and 132 reflect higher v_A levels with turning points that align with $v_X = 0$ (*B* and *B′*). For $\alpha_0 = 1.0$, both X and A potential curves acquire much deeper wells with similar R_m, show only 0 → 0 transition, shortest but most intense.

Discussion and Outlook

In realm I, we considered the interaction of nonresonant laser fields with the polarizability of the ground electronic state ($X^1\Sigma_g^+$) of the helium dimer (Figs. 1–4 and Table 2). The field-free dimer has only one barely bound vibrational level; in kelvin units, it lies only about 10^{-3} K below the He + He dissociation asymptote. The laser field enhances the molecular binding, but the sole level remains in the van der Waals range. For example, applying laser intensity of 3×10^{14}W/cm^2 merely lowers the location of the sole level to about 10 K. However, such laser intensity interacting with the anisotropy of the polarizability constrains the dimer axis to pendular librating motion within ±27°, a rather narrow range (Fig. 4). Accordingly, the sole bound level is appropriately designated penvib. Our chief concerns dealt with three issues mutually involved: (*i*) the key role of the laser pulse duration (Fig. 5); (*ii*) intrusion of ionization; and (*iii*) the centrifugal energy associated with the sole penvib level. The outcome, not anticipated, emerged that the laser interaction lowered the penvib level enough to offset the centrifugal input, hence avoiding dissociation.

Table 2. Laser-induced parameters for ground state of $^4He_2$ dimer

I, a.u.	I, W/cm^2	V, R_m	R_m	$\langle R\rangle$	E_0, a.u.	E_0, K
0	0	3.5×10^{-5}	5.61	97.9	-4.1×10^{-9}	−0.0013
0.002	7.0×10^{13}	5.5×10^{-5}	5.53	25.5	-1.9×10^{-7}	−0.061
0.005	1.8×10^{14}	8.6×10^{-5}	5.45	9.8	-3.8×10^{-6}	−1.2
0.010	3.5×10^{14}	1.4×10^{-4}	5.35	7.5	-2.0×10^{-5}	−6.3
0.015	5.3×10^{14}	2.0×10^{-4}	5.28	6.8	-4.4×10^{-5}	−13.8
0.020	7.0×10^{14}	2.5×10^{-4}	5.22	6.5	-7.3×10^{-5}	−23.0

Quantities in atomic units (except as noted). $V(R_m)$ and $\langle R\rangle$ pertain to $\theta=0°$.

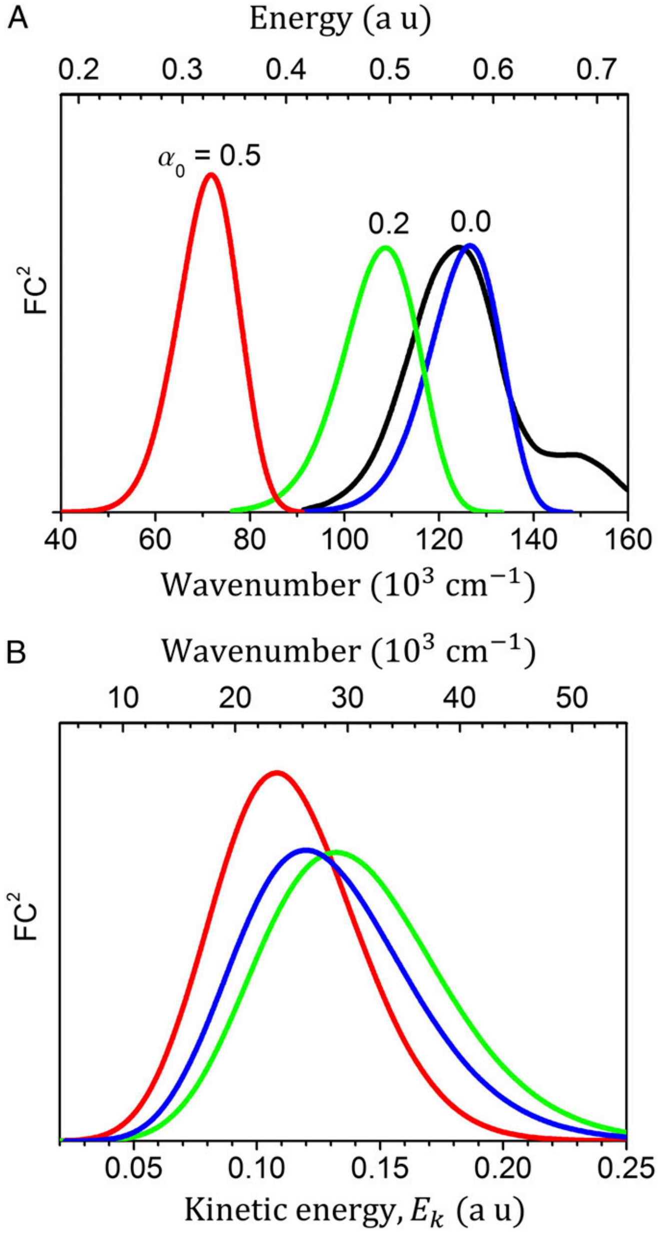

Fig. 10. Internal photodissociation of He_2 dimer. (*A*) Franck–Condon (FC) continuum transitions from KH potentials for $\alpha_0=0, 0.2, 0.5$ (blue, green, red; Fig. 9*A*) compared with field-free spectrum (black profile). Notation FC^2 designates sum of squares of $\langle v_A|v_X\rangle$. (*B*) Corresponding kinetic energy carried off as the pair of helium atoms fly apart. The predicted exit velocity of each He atom at the peak distribution for $\alpha_0=0, 0.2, 0.5$ are similar: 12.5, 13.6, 11.9 km/s, respectively.

In realm II, abundant theoretical work has adopted the KH approach since it emerged 50 y ago (45). However, experimental confirmation for KH effects has been meager, limited mostly to Rydberg atoms until the recent decade (54, 55). As yet, experimental affirmation is still lacking for molecules, particularly the helium dimer. Previous theoretical pursuits of KH dressing have all dealt with the ground electronic state, assessing bond energies, molecular orbitals, and vibrational and rotational levels (13–15). We have introduced the excited electronic state ($A^1\Sigma_u^+$) to provide more accessible experimental tests with a wide range of discrete and continuum spectra (Figs. 6–10 and Table 1). In particular, the transitions between the X and A states occur in times much shorter than molecular rotation or pendular motion, so the transition dipole moment aligns with the electric vector of the light (56). Accordingly, in the continuum spectra the laser polarization supplies a distinctive angular distribution of the departing atoms.

Realms I and II share the same experimental techniques in producing a molecular beam of the helium dimer and detecting it. In an elegant procedure, a pure helium dimer beam cooled to 8 K has been obtained by matter wave diffraction (8). Also elegant is detecting the beam by ionizing singly the atoms, so the two positively charged atoms repel, resulting in a Coulomb explosion. Recording the momentum vectors of the ions provides velocity and directional data. The process was recently exemplified for the dimer field-free X state by imaging the wavefunction and binding (8). It has been used also to study nonadiabatic alignment of the dimer (27). The imaging process noted in our discussion of A–X internal photodissociation does not require a Coulomb explosion (30). These particle-imaging techniques can now cope with the continuum spectra while well-established pump–probe techniques deal with the discrete spectra in elucidating the KH regime.

Methods

In realm I, a self-consistent stepwise iterative method was used to obtain the penvib states from Eq. **2**. Radial and pendular parts of the equation were solved separately. In realm II, RHF and CIS methods were used to obtain potential surfaces of $X^1\Sigma_g^+$ and $A^1\Sigma_u^+$ states from Eq. **6**. The method used for penvib states in realm II is the same as that in realm I.

ACKNOWLEDGMENTS. Q.W. thanks Konstantin Dorfman for enlightening discussion of lasers. We are grateful for support from National Natural Science Foundation of China (Grant 11674098) and Institute for Quantum Science and Engineering, Texas A&M University.

1. Anderson JB, Trynor CA, Boghosian BM (1993) An exact quantum Monte Carlo calculation of the helium-helium intermolecular potential. *J Chem Phys* 99:345–351.
2. Tang KT, Toennies JP, Yiu CL (1995) Accurate analytical He-He van der Waals potential based on perturbation theory. *Phys Rev Lett* 74:1546–1549.
3. Przybytek M, et al. (2010) Relativistic and quantum electrodynamics effects in the helium pair potential. *Phys Rev Lett* 104:183003.
4. Lou F, McGane GC, Kirn G, Giese CF, Gentry WR (1993) The weakest bond: Experimental observation of the helium dimer. *J Chem Phys* 98:3564–3567.
5. Luo F, Giese CF, Gentry WR (1996) Direct measurement of the size of the helium dimer. *J Chem Phys* 104:1151–1154.
6. Schollkopf W, Toennies JP (1996) The nondestructive detection of the helium dimer and trimer. *J Chem Phys* 104:1155–1158.
7. Grisenti RE, et al. (2000) Determination of the bond length and binding energy of the helium dimer by diffraction from a transmission grating. *Phys Rev Lett* 85:2284–2287.
8. Zeller S, et al. (2016) Imaging the He_2 quantum halo state using a free electron laser. *Proc Natl Acad Sci USA* 113:14651–14655.
9. Zemke WT, Byrd JN, Michels HH, Montgomery JA, Jr, Stwalley WC (2010) Long range intermolecular interactions between the alkali diatomics $Na_{(2)}$, $K_{(2)}$, and NaK. *J Chem Phys* 132:244305.
10. Jensen AS, Rusagr K, Fedorov DV (2004) Structure and reactions of quantum halos. *Rev Mod Phys* 76:215–261.
11. Komasa J (2001) Exponentially correlated Gaussian functions in variational calculations. Momentum space properties of the ground state helium dimer. *J Chem Phys* 115:158–165.
12. Focsa C, Bernath PF, Colin R (1998) The low-lying states of He_2. *J Mol Spectrosc* 191: 209–214.
13. Yasuike T, Someda K (2004) He-He chemical bonding in high-frequency intense laser fields. *J Phys B At Mol Opt Phys* 37:3149–3162.
14. Wei Q, Kais S, Herschbach D (2008) Dimensional scaling treatment of stability of simple diatomic molecules induced by superintense, high-frequency laser fields. *J Chem Phys* 129:214110.
15. Balanarayan P, Moiseyev N (2012) Strong chemical bond of stable He_2 in strong linearly polarized laser fields. *Phys Rev A* 85:032516.
16. Friedrich B, Herschbach D (1995) Alignment and trapping of molecules in intense laser fields. *Phys Rev Lett* 74:4623–4626.
17. Friedrich B, Herschbach D (1995) Polarization of molecules induced by intense nonresonant laser fields. *J Phys Chem* 99:15686–15693.
18. Seideman T (1995) Rotational excitation and molecular alignment in intense laser fields. *J Chem Phys* 103:7887–7896.
19. Ortigoso J, Rodriguez M, Gupta M, Friedrich B (1999) Time evolution of pendular states created by the interaction of molecular polarizability with a pulsed nonresonant laser field. *J Chem Phys* 110:3870–3875.
20. Stapelfeldt H, Seideman T (2003) Colloquium: Aligning molecules with strong laser pulses. *Rev Mod Phys* 75:543–557.
21. Torres R, de Nalda R, Marangos JP (2005) Dynamics of laser-induced molecular alignment in the impulsive and adiabatic regimes: A direct comparison. *Phys Rev A* 72: 023420.
22. Condon EU (1932) Production of infrared spectra with electric fields. *Phys Rev* 41: 759–762.
23. Parker JS, Meharg KJ, McKenna GA, Taylor KT (2007) Single-ionization of helium at Ti: Sapphire wavelengths: Rates and scaling laws. *J Phys B At Mol Opt Phys* 40:1729–1743.
24. Friedrich B, Gupta M, Herschbach D (1998) Probing weakly bound species with nonresonant light: Dissociation of He_2 induced by rotational hybridization. *Collect Czech Chem Commun* 63:1089–1093.
25. Lemeshko M, Friedrich B (2009) Probing weakly bound molecules with nonresonant light. *Phys Rev Lett* 103:053003.
26. Lemeshko M, Friedrich B (2009) Rotational and rotationless states of weakly bound molecules. *Phys Rev A* 79:050501.
27. Kunitski M (2018) Rotating rotationless: Nonadiabatic alignment of the helium dimer (Goethe Universitat, Frankfurt Am Main), in press.
28. Yan ZC, Seideman T (1999) Photomanipulation of molecular modes: A time-dependent self-consistent-field approach. *J Chem Phys* 111:4113–4120.
29. Weber MJ (1999) *Handbook of Laser Wavelengths* (CRC Press, Boca Raton, FL).
30. Chandler DW, Houston PL, Parker DH (2017) Perspective: Advanced particle imaging. *J Chem Phys* 147:013601.
31. Gavirla M, ed (1992) *Atoms in Intense Laser Fields* (Academic, New York).
32. Eberly JH, Kulander KC (1993) Atomic stabilization by super-intense lasers. *Science* 262:1229–1233.
33. Gavila M (2002) Topical review: Atomic stabilization in superintense laser fields. *J Phys B At Mol Opt Phys* 35:R147–R193.
34. van Duijn E, Gavrila M, Muller HG (1996) Multiply charged negative ions of hydrogen induced by superintense laser fields. *Phys Rev Lett* 77:3759–3762.
35. Wei Q, Kais S, Moiseyev N (2006) New stable multiply charged negative atomic ions in linearly polarized superintense laser fields. *J Chem Phys* 124:201108.
36. Wei Q, Kais S, Moiseyev N (2007) Frequency-dependent stabilization of He^- by a superintense laser field. *Phys Rev A* 76:013407.
37. Wei Q, Kais S, Herschbach D (2007) Dimensional scaling treatment of stability of atomic anions induced by superintense, high-frequency laser fields. *J Chem Phys* 127: 094301.
38. Wei Q, Herschbach D (2013) Positronium in superintense high-frequency laser fields. *Mol Phys* 111:1835–1843.
39. Balanarayan P, Moiseyev N (2013) Chemistry in high-frequency strong laser fields: The story of HeS molecule. *Mol Phys* 111:1814–1822.
40. Smirnova O, Spanner M, Ivanov M (2003) Molecule without electrons: Binding bare nuclei with strong laser fields. *Phys Rev Lett* 90:243001.
41. Kapitza PI (1965) *Collected Papers*, ed Ter Haar D (Pergamon, Oxford), Vol 2.
42. Paul W (1990) Electromagnetic traps for charged and neutral particles. *Rev Mod Phys* 62:531–540.
43. Hau LV, Burns MM, Golovchenko JA (1992) Bound states of guided matter waves: An atom and a charged wire. *Phys Rev A* 45:6468–6478.
44. Kramers HA (1956) *Collected Scientific Papers* (North-Holland, Amsterdam), p 866.
45. Henneberger WC (1968) Perturbation method for atoms in intense light beams. *Phys Rev Lett* 21:838–841.
46. Schmidt MW, et al. (1993) General atomic and molecular electronic structure system. *J Comput Chem* 14:1347–1363.
47. Foreman JB, Head-Gordon M, Pople JA, Frisch MJ (1992) A systematic molecular orbital theory for excited states. *J Phys Chem* 96:135–149.
48. Shertzer J, Chandler A, Gavrila M (1994) H_2^+ in superintense laser fields: Alignment and spectral restructuring. *Phys Rev Lett* 73:2039–2042.
49. Nguyen NA, Nguyen-Dang T-T (2000) Molecular dichotomy within an intense high-frequency laser field. *J Chem Phys* 112:1229–1239.
50. Yasuike T, Someda K (2008) Lifetime of metastable helium molecule in intense laser fields. *Phys Rev A* 78:013403.
51. Pellegrini C, Marinelli A, Reiche S (2016) The physics of x-ray free-electron lasers. *Rev Mod Phys* 88:015006.
52. Gardner D, et al. (2017) Sub-wavelength coherent imaging of periodic samples using a 13.5 nm tabletop high harmonic light source. *Nat Photonics* 11:259–263.
53. Hill PC (1989) Ultraviolet continua of helium molecules. *Phys Rev A Gen Phys* 40: 5006–5016.
54. Morales F, Richter M, Patchkovskii S, Smirnova O (2011) Imaging the Kramers-Henneberger atom. *Proc Natl Acad Sci USA* 108:16906–16911.
55. Wei Q, Wang P, Kais S, Herschbach D (2017) Pursuit of the Kramers-Henneberger atom. *Chem Phys Lett* 683:240–246.
56. Zare RN, Herschbach DR (1963) Doppler line shape of atomic fluorescence excited by molecular dissociation. *Proc IEEE* 51:173–182.